ADVANCED FUNCTIONAL MATERIALS

Supporting Information

for *Adv. Funct. Mater.,* DOI: 10.1002/adfm.202107160

Designing Porous Antifouling Interfaces for High-Power Implantable Biofuel Cell

Lie Wang, Er He, Rui Gao, Xiaotong Wu, Anwei Zhou, Jiang Lu, Tiancheng Zhao, Jiaxin Li, Yanjing Yun, Luhe Li, Tingting Ye, Yiding Jiao, Jiacheng Wang, Hao Chen, Dan Li, Xinghai Ning, Di Wu, Huisheng Peng, and Ye Zhang**

Supporting Information

1. Preparation of carbon nanotube (CNT) fiber

The CNT fiber was synthesized *via* floating catalyst chemical vapor deposition with thiophene (1–2 wt%) and ferrocene (1–2 wt%) as the catalysts and flowing ethanol (97 wt%), Ar (200 sccm) and H_2 (2000 sccm) as carbon source, carrier gas and reduction gas, respectively. CNT aerogel was first produced continuously at the hot zone (1200 °C) of a tube furnace and then collected into a cylindrical hollow sock. After that, the CNT sock was pulled out of the furnace by a titanium rod and shrank into the CNT ribbon through water and ethanol in turn. It was finally washed by acetone for further densification, followed by drying, twisting and collecting onto a spool to produce the CNT fiber.

2. Fabrication of glucose electrochemical sensor

A multi-step electrochemical procedure was used to fabricate the glucose electrochemical sensor. Firstly, polyaniline (PANI) was deposited by the chronoamperometry method at 0.75 V for 20 seconds in a three-electrode system. The aqueous electrolyte included 0.5 M aniline and 1 M H_2SO_4. The CNT fiber, commercial Pt and Ag/AgCl were used as working, counter and reference electrodes, respectively. Secondly, Pt nanoparticles were deposited onto CNT/PANI fiber by an electrochemical double potential step method. The first step was at 0.5 V for 10 seconds and the second step was at -0.7 V for 10 seconds, and the whole process included 50 cycles. The aqueous electrolyte included 0.1 M KCl and 1 mM K_2PtCl_6. The CNT/PANI fiber, commercial Pt and Ag/AgCl were used as working, counter and reference electrodes, respectively. Thirdly, the glucose-responsive layer was coated onto the CNT/PANI/Pt fiber. A mixed solution with 0.7 mL PVA, 0.3 mL PVA-SbQ and 0.1 mL GOx solution (30 $U \cdot mL^{-1}$) were stirred at room temperature for 2 hours to obtain GOx based PAI precursor solution. The GOx based PAI precursor solution (4 μL) was dipped onto the CNT/PANI/Pt fiber, followed by photopolymerizing under a UV lamp (λ = 365 nm, 10 minutes) at room temperature. Finally, the glucose electrochemical sensor was obtained by gently washing it with PBS solution and drying overnight at 4 ^oC.

3. Characterization

3.1. Structures and morphologies

The structures and morphologies were characterized by scanning electron microscopy

(SEM, Hitachi FE-SEM S-4800), atomic force microscope (AFM, Bruker ICON), micropore specific surface area analyzer (Kubo, X100), fluorescence microscope (Axio Vert A1), Raman spectrometer (HORIBA Ltd. LabRAM HR Evolution), and Fourier transform infrared spectroscopy (Bruker Tensor 27). The photographs were taken by a camera (Nikon, J1).

3.2. Mechanical characterization

The bending stiffness (*D*) of the fiber electrode was calculated by:

$$D = E \times I$$

Where *E* and *I* are the elastic modulus and moment of inertia, respectively. For a fiber with a diameter of *d*, the moment of inertia was calculated by:

$$I = \frac{\pi d^4}{64}$$

The modulus was measured by nanoindentation experiments performed using a spring constant of 0.06 $N \cdot m^{-1}$ and a microsphere of 0.6 μm in diameter. The deflection sensitivity of the AFM cantilever was calibrated on a stiff substrate (Si) before the nanoindentation experiment on the fiber. The nanoindentation hardness and reduced modulus were calculated from the unloading part in the load-displacement curve (**Figure S4a**) using the Sneddon model:

$$F = \frac{2}{\pi} \times \frac{E}{\pi \times (1 - v^2)} \times \delta^2$$

Where *F* and δ are the loading force and indentation depth in the elastic regime, respectively; *v* is the Poisson ratio, which was set to be 0.5. The tests were repeated at least three times.

3.3 Live or Death™ cell viability test

BFC-PAI films were cut down into small sizes by about 2 mm×2 mm and were placed into a 96-well plate after sterilization. When cell cultivation, 0.5 mL suspended L929 (1×10^5 cell·mL^{-1}, Nanjing Herbal Source Biotechnology Co., Ltd.) or human umbilical vein endothelial cells (HUVEC, 1×10^5 cell • mL^{-1}, iCell Bioscience Inc, Shanghai) were seeded into 96-well plates, one with BFC-PAI films and the other with glass as a control group. Both groups were cultivated under 37 ^oC and 5% CO_2 for 1 d and taken for CCK-8 test (CK04). For CCK-8 test, 10 μL CCK-8 was added to each well. The samples were analyzed using a UV-vis spectrophotometer (TECAN, infinite M200 PRO) at the wavelength of 450 nm after incubating for 1 hour. The tests were repeated at least three times. Statistical significance was calculated using

unpaired Student’s t-test. NS represents $p > 0.05$.

Furthermore, BFC-PAI and control group of cells were taken for Calcein/propidium iodide (Calcein/PI) cell viability/cytotoxicity assay after cultivated in a 24-well plate (3×10^5 cell·mL^{-1}) for 1 day. For Calcein/PI cell viability/cytotoxicity assay, 250 μL Calcein/PI was added to each well. After incubated at 37 ^{o}C for 45 minutes without contacting light, cells were washed with PBS solution twice. Cells were monitored under fluorescence microscope (Axio Vert A1).

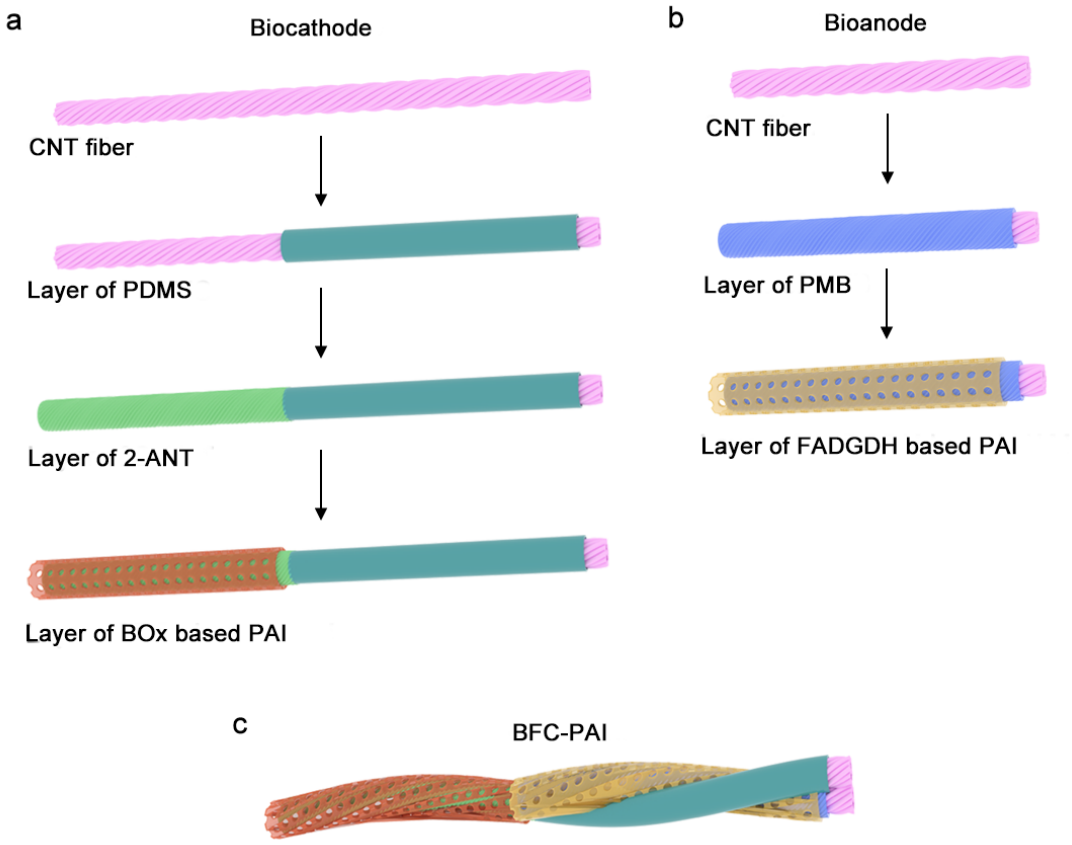

Figure S1. Schematic illustration of the fabrication of **(a)** biocathode and **(b)** bioanode. **(c)** Schematic illustration of the structure of BFC-PAI.

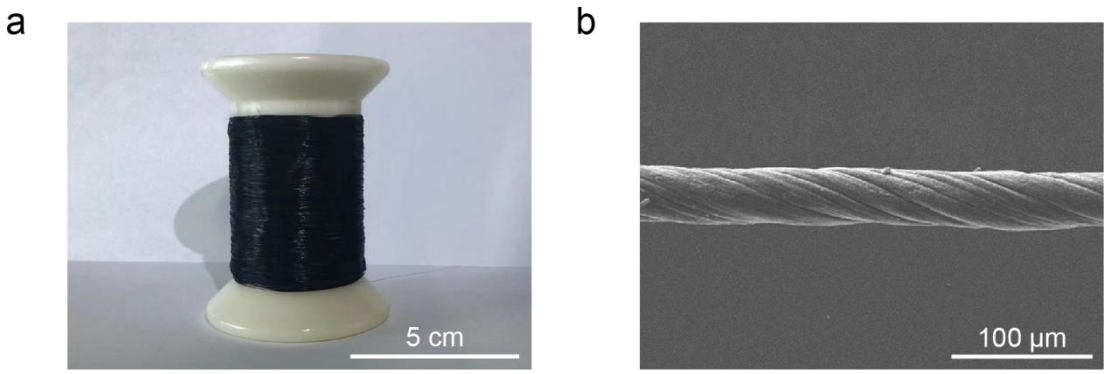

Figure S2. (a) Photograph and **(b)** SEM image of the CNT fiber.

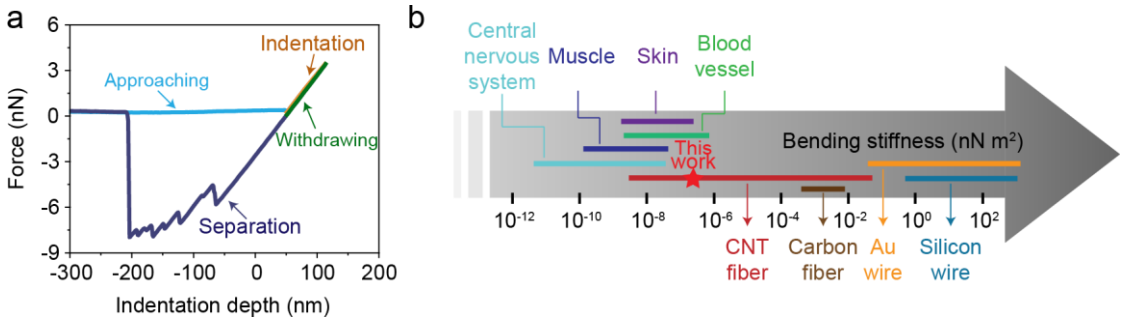

Figure S3. Mechanical match of the CNT fiber. **(a)** Nanoindentation curves on CNT fiber. Bending stiffness of 4.2×10^{-7} nN·m^2 was calculated by fitting the indentation curve. **(b)** Comparison of the CNT fiber with other implantable materials and tissues. The other data were cited from Ref.[1]

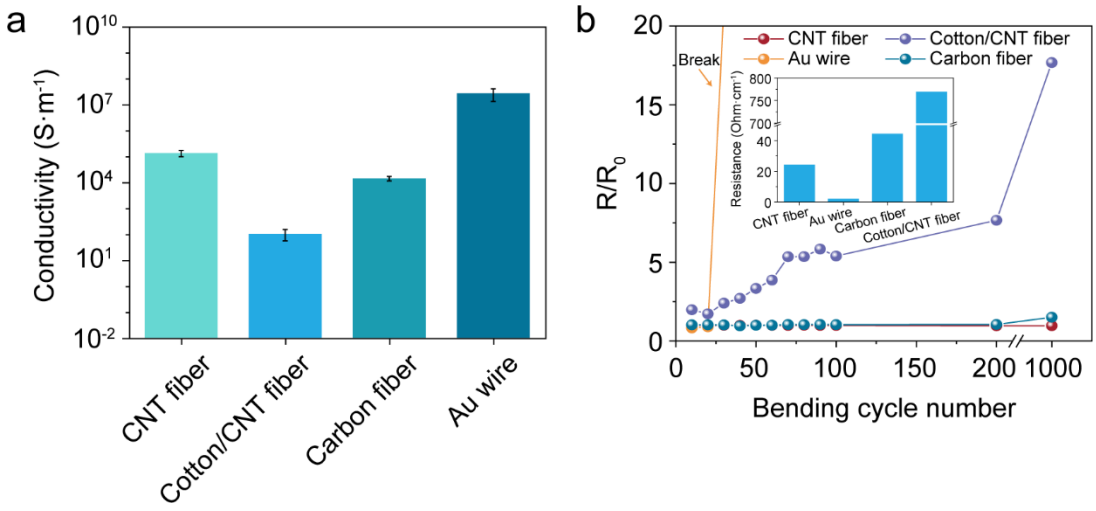

Figure S4. Electrical conductivity of CNT fiber. **(a)** The conductivity of CNT fiber compared with Au wire, carbon fiber and cotton/CNT fiber. The inserted photographs display the corresponding fiber with length of 2 cm. **(b)** Electrical resistance of the CNT fiber is maintained after bending for 1,000 cycles, superior to Au wire, carbon fiber, and cotton/CNT fiber. Here R_0 and R correspond to electrical resistances before and after bending, respectively.

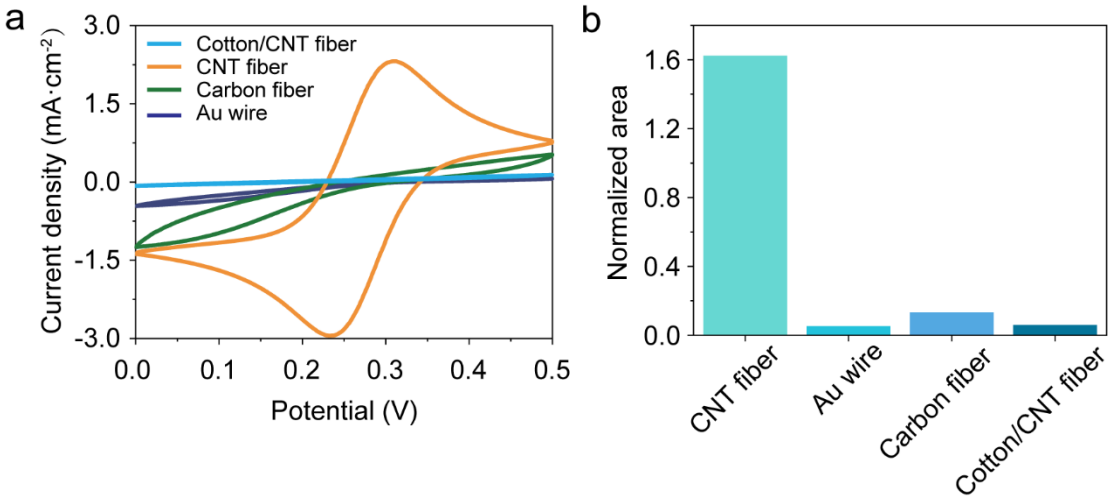

Figure S5. The electrochemically active surface area of CNT fiber compared with other fiber electrodes. **(a)** Cyclic voltammetry plots of four fiber electrodes in 1 mM KCl solution with 5 mM $K_4Fe(CN)_6/K_3Fe(CN)_6$ (scan rate of 100 $mV \cdot s^{-1}$ between 0 and 0.5 V). **(b)** Normalized areas of different fiber electrodes. The data were calculated according to the CV plots.

The CNT fiber electrodes played an essential role in the high performance of BFC-PAI due to the combined high mechanical, electrical and electrochemical properties. For example, they exhibited bending stiffness of about 4.2×10^{-7} $nN \cdot m^2$, which could be adapted to the range of most tissues, such as muscles and blood vessels (**Figure S3**). They also showed electrical conductivity of about 10^5 $S \cdot m^{-1}$, and the electrical resistance had been well maintained after bending for 1,000 cycles, which was superior to the other flexible electrodes such Au wire, carbon fiber and cotton/CNT composite fiber (**Figure S4**). According to the Randles-Sevcik equation, the electrochemically active surface area of the CNT fiber was further estimated by cyclic voltammetry (CV) in $Fe(CN)_6^{4-}$ solution. As shown in **Figure S5**, the CNT fiber exhibited a normalized area (effective electrochemically active surface area/geometric surface area) of ~1.62, which was 32 times of Au wire, 12 times of carbon fiber and 28 times of cotton/CNT fiber. Therefore, the CNT fiber was advantageous for the deposition of different functional materials, aiming at a high-performance implantable BFC.

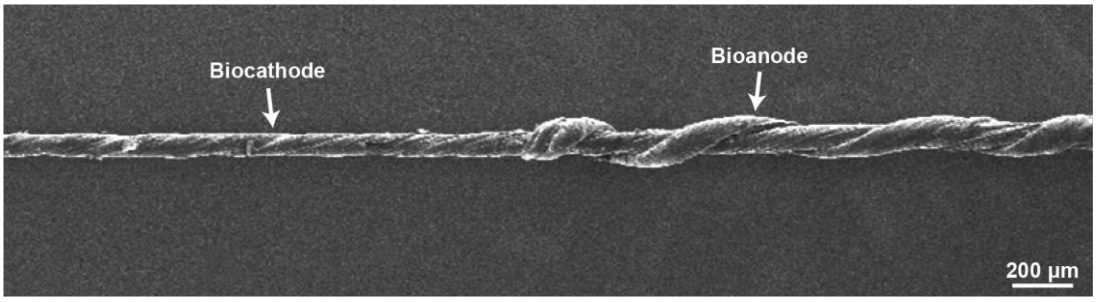

Figure S6. SEM image of the BFC-PAI.

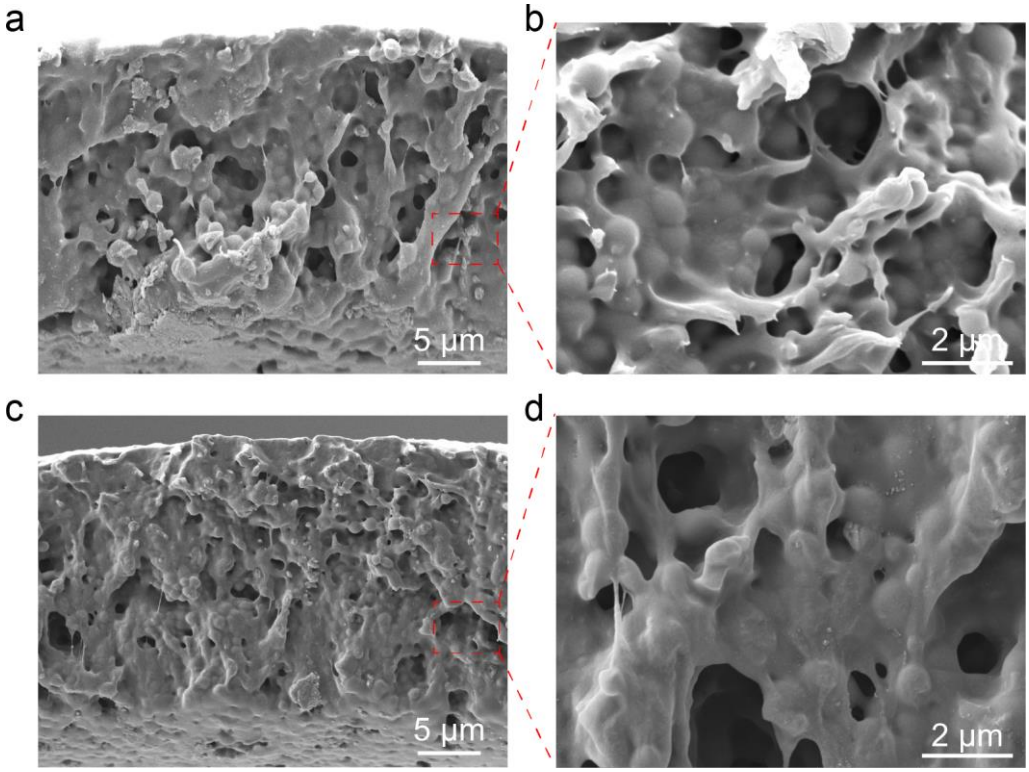

Figure S7. SEM image by side view at the cross section of the PAI on (**a**, **b**) biocathode and (**c**, **d**) bioanode.

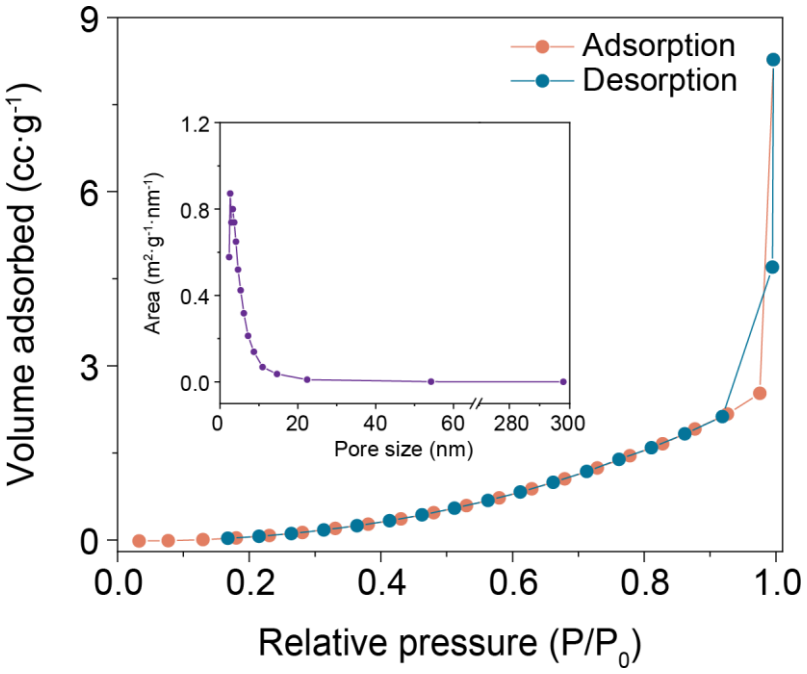

Figure S8. Nitrogen adsorption isotherm of PAI. Insert: pore size distribution of PAI calculated after fitting Barrett-Joyner-Halenda (BJH) models to nitrogen gas adsorption data.

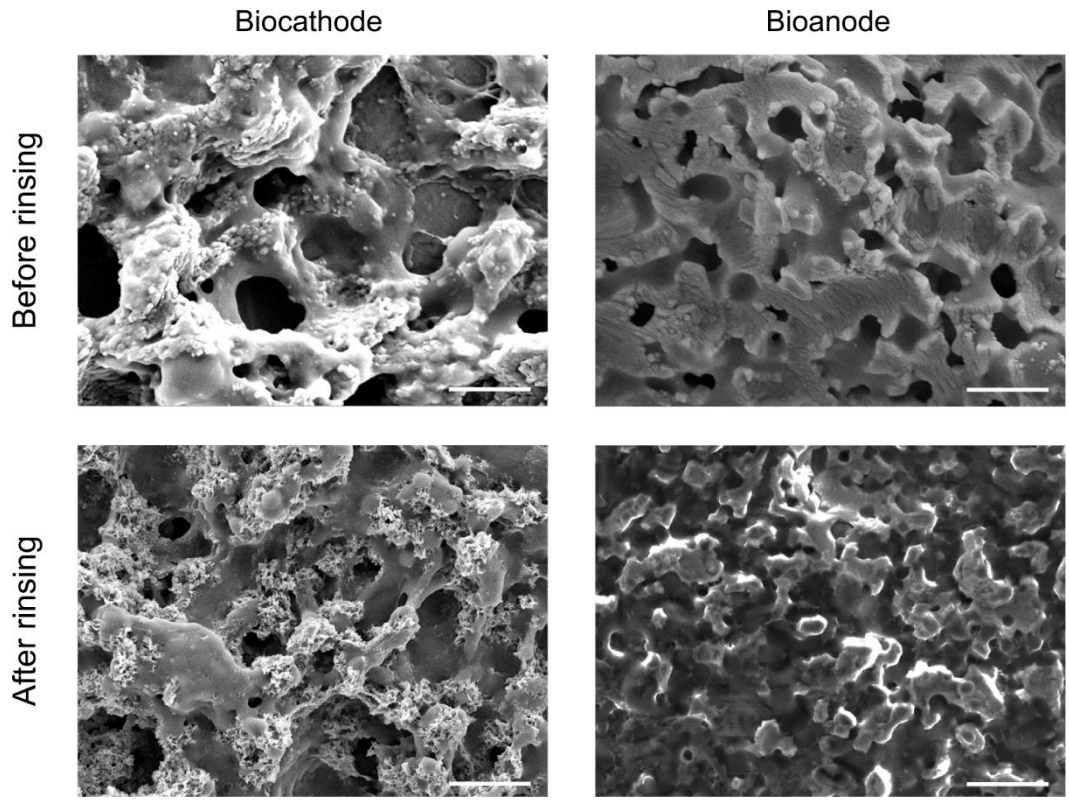

Figure S9. SEM images of the bioelectrodes prepared with PAI before and after rinsing. Scale bar, 2 μm.

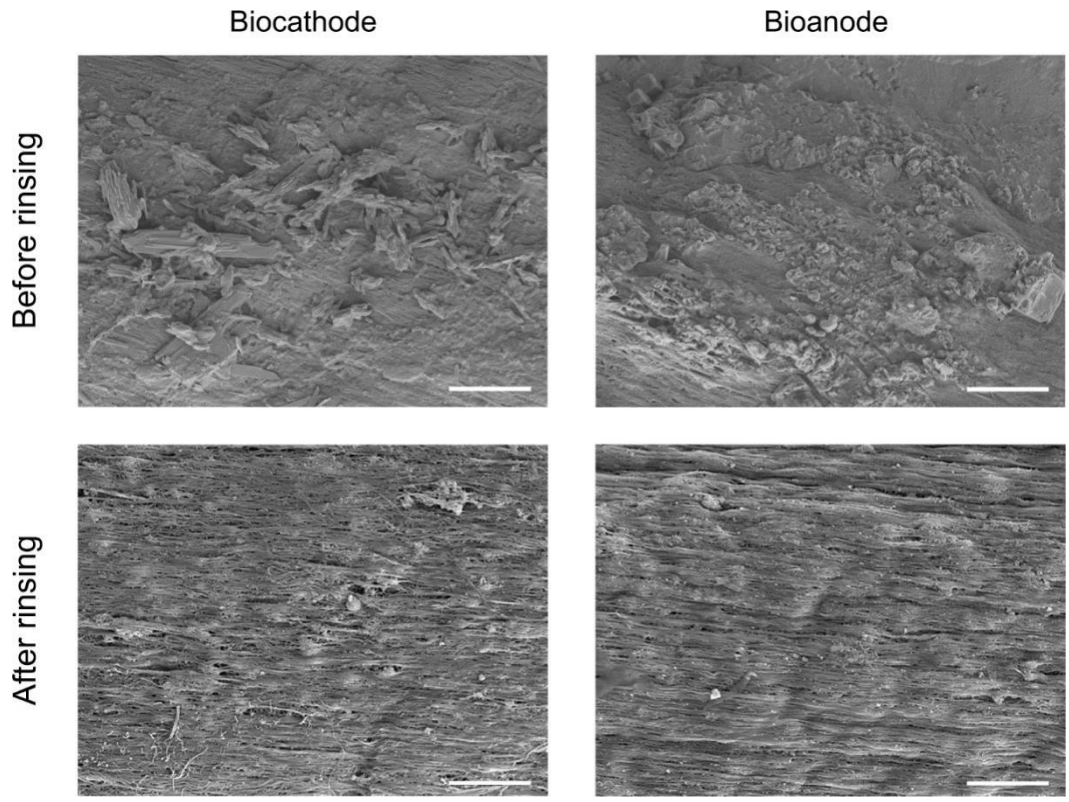

Figure S10. SEM images of the bioelectrodes prepared without PAI before and after rinsing. Scale bar, 2 μm.

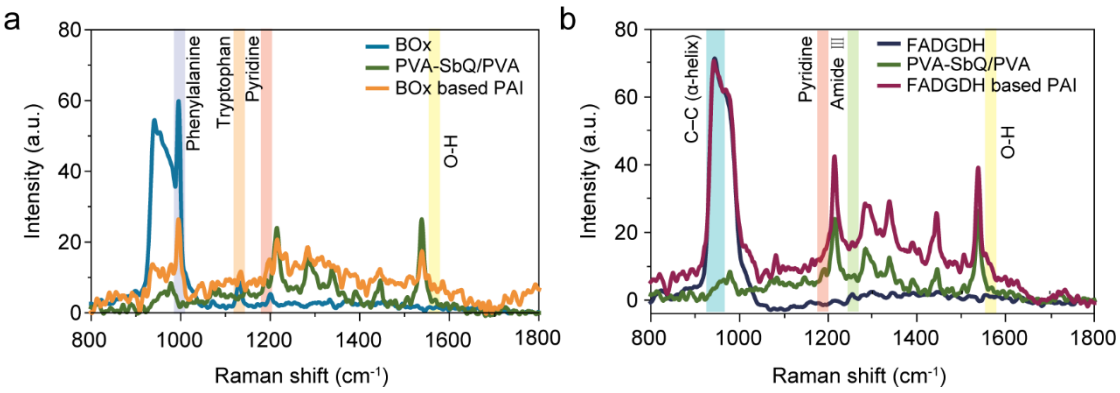

Figure S11. Raman spectra of **(a)** BOx based PAI and **(b)** FADGDH based PAI.

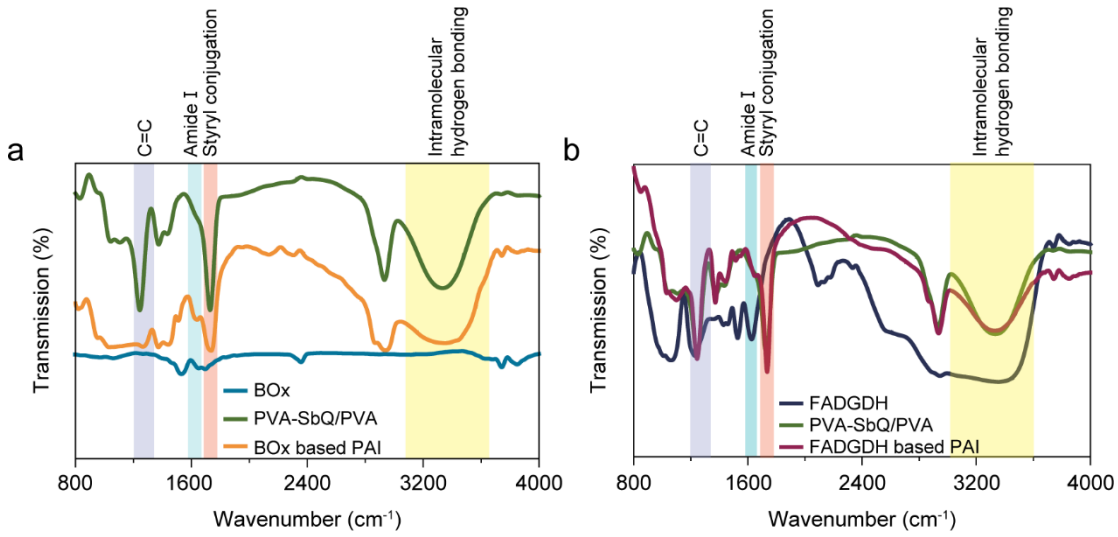

Figure S12. Fourier spectra of **(a)** BOx based PAI and **(b)** FADGDH based PAI.

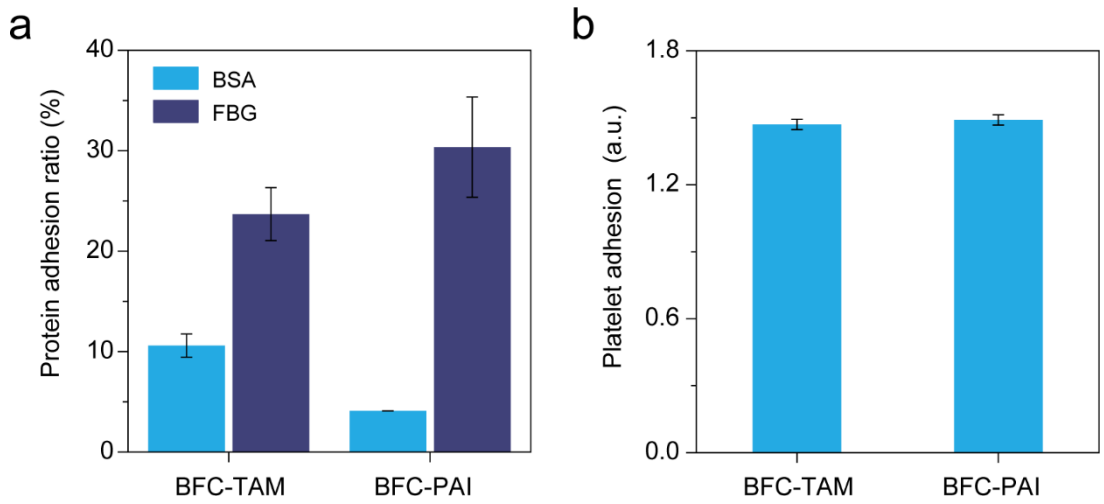

Figure S13. (a) BSA adhesion and FBG adhesion ratio, and **(b)** platelet adhesion of BFC-PAI and BFC prepared with traditional PVA antifouling coating (denote as BFC-TAM).

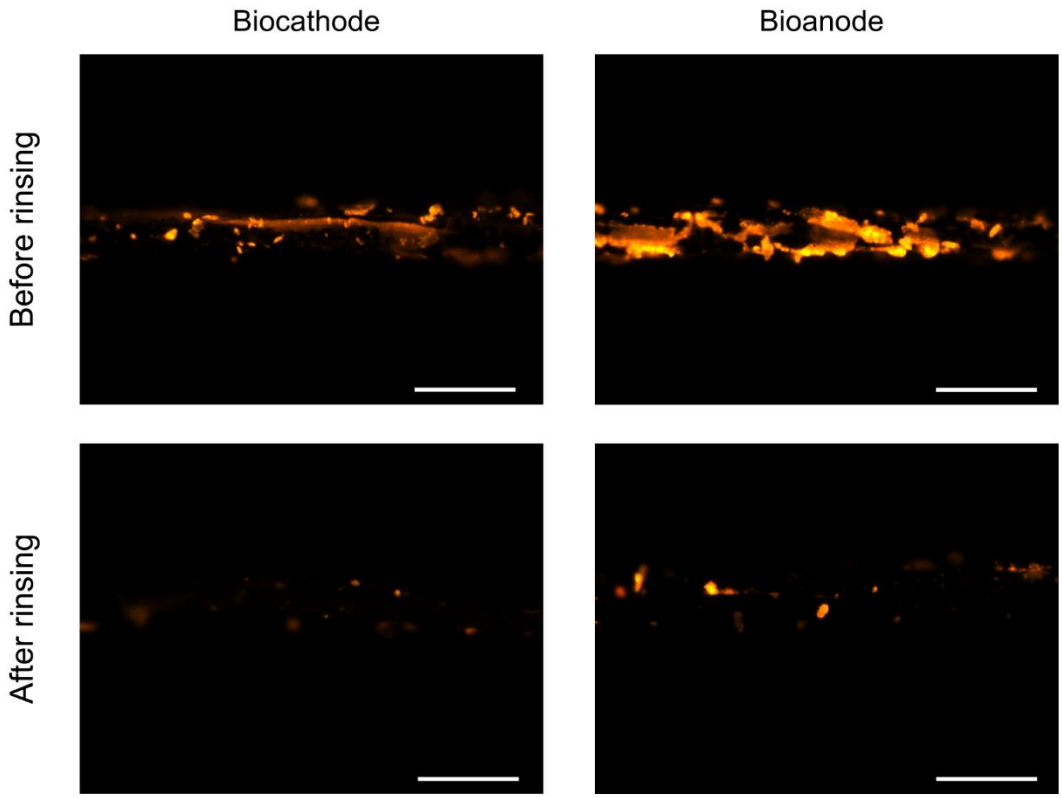

Figure S14. Fluorescence images of enzyme immobilization on the electrode with PVA before and after rinsing with PBS solution. Scale bar, 50 μm.

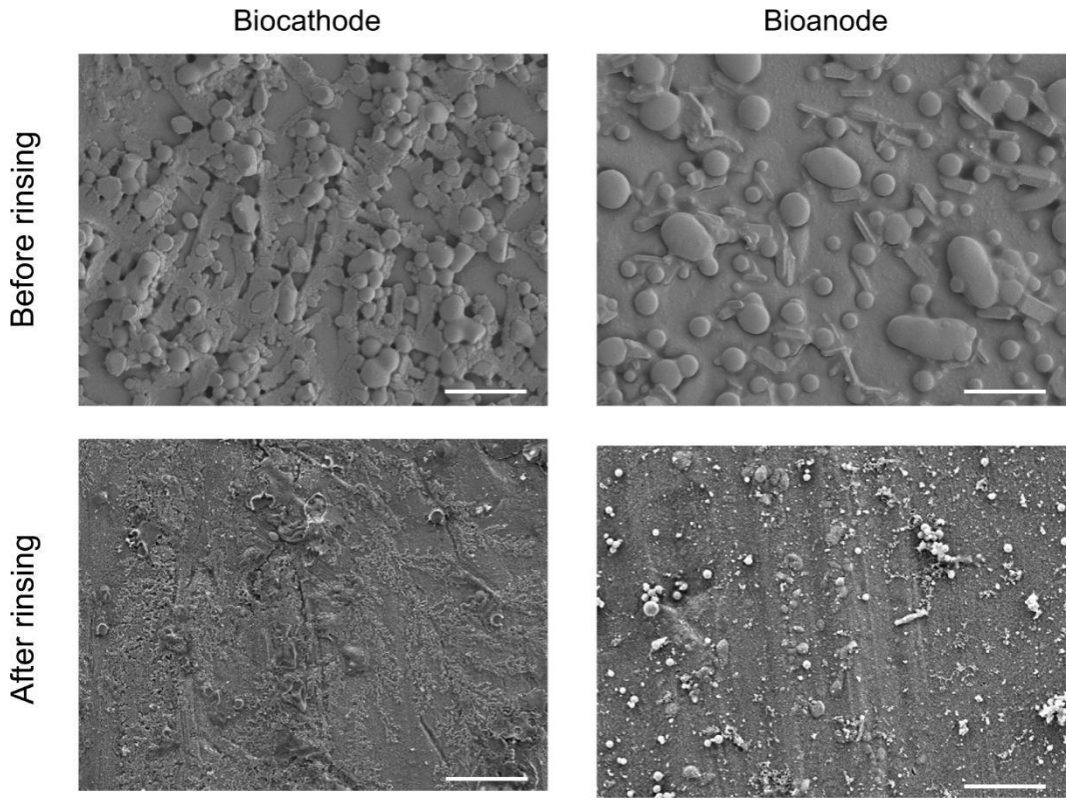

Figure S15. SEM images of the bioelectrodes prepared with PVA before and after rinsing. Scale bar, 2 μm.

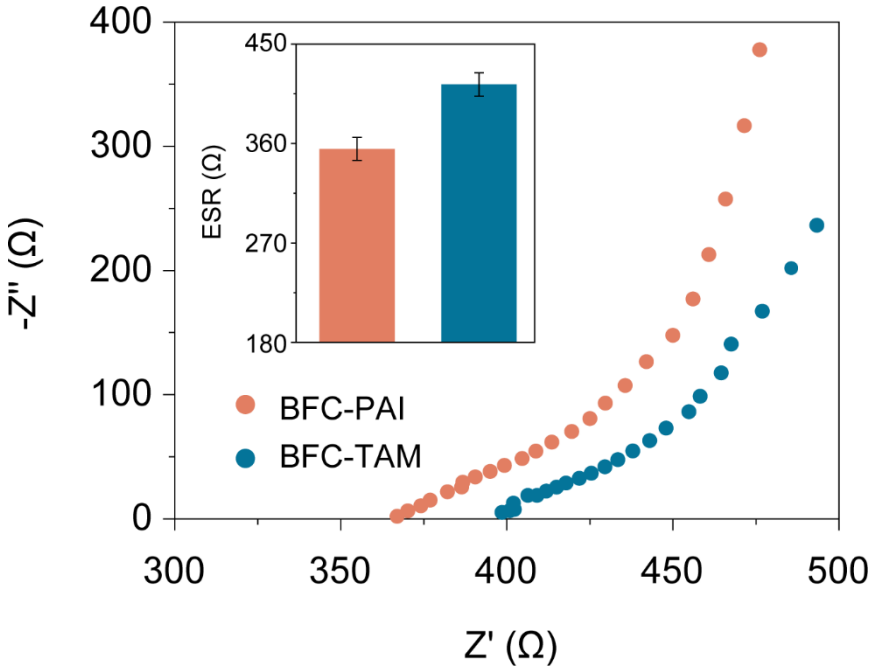

Figure S16. Nyquist plots and the equivalent series resistance (ESR, inset) of BFC-PAI and BFC-TAM tested in blood.

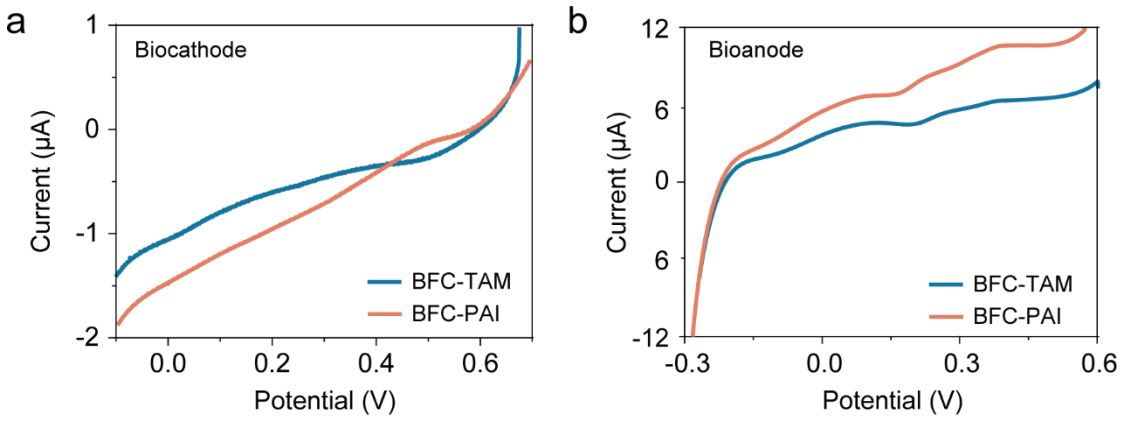

Figure S17. Linear cyclic voltammetry plots of two different biocathodes or bioanodes. **(a)** Bioelectrocatalytic reduction of O_2 by biocathode of BFC-TAM and BFC-PAI in blood. **(b)** Bioelectrocatalytic oxidation of glucose by biocathode of BFC-TAM and BFC-PAI in blood.

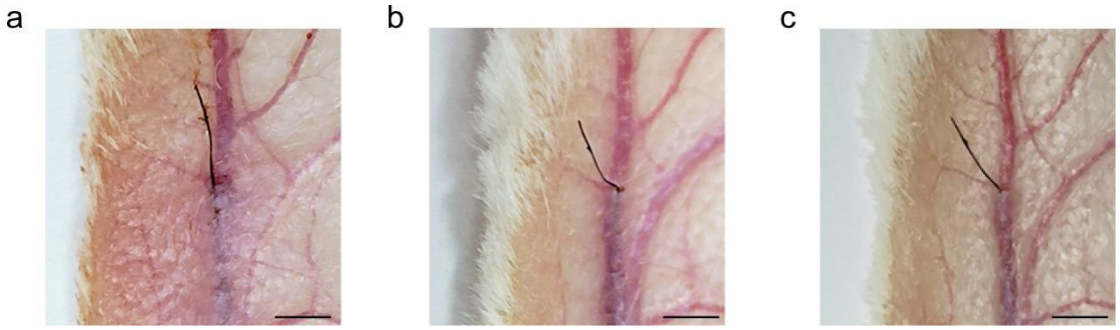

Figure S18. Representative optical images of the BFC-PAI implanted in the vein of a rabbit for **(a)** 1 day, **(b)** 5 days and **(c)** 7 days, showing no inflammation in all cases. The wound around the injected CNT fiber on the skin surface was only tens of micrometers larger than the radius of the fiber after injection and usually recovered within 10 minutes. No sign of infection or abnormality was detected during 7 days after the injection. Scale bar, 500 μm.

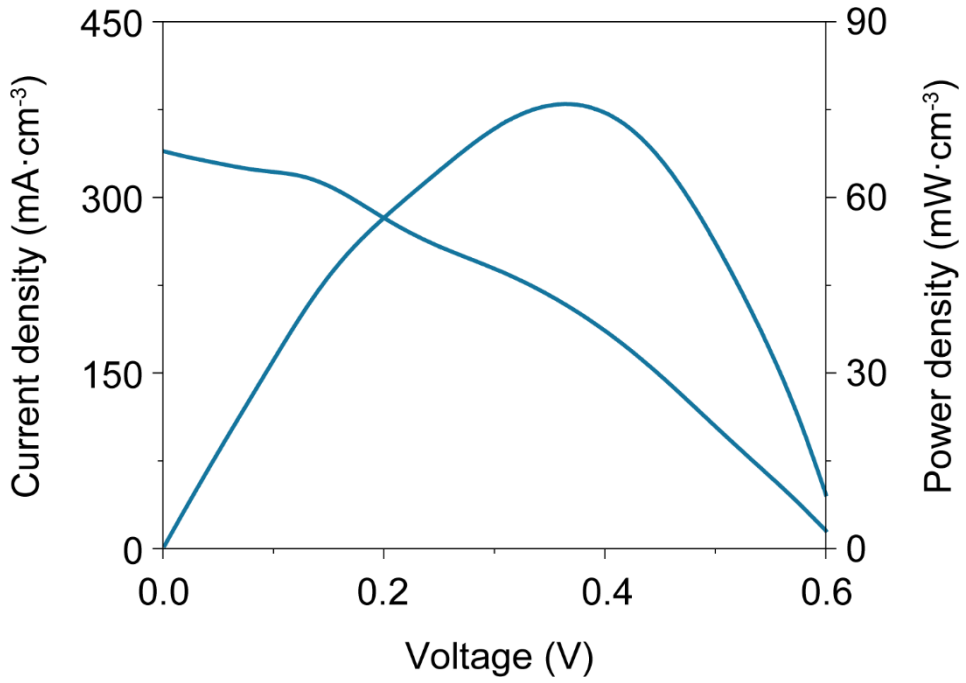

Figure S19. Polarization curves and power density curves of the bare BFC tested in PBS solution.

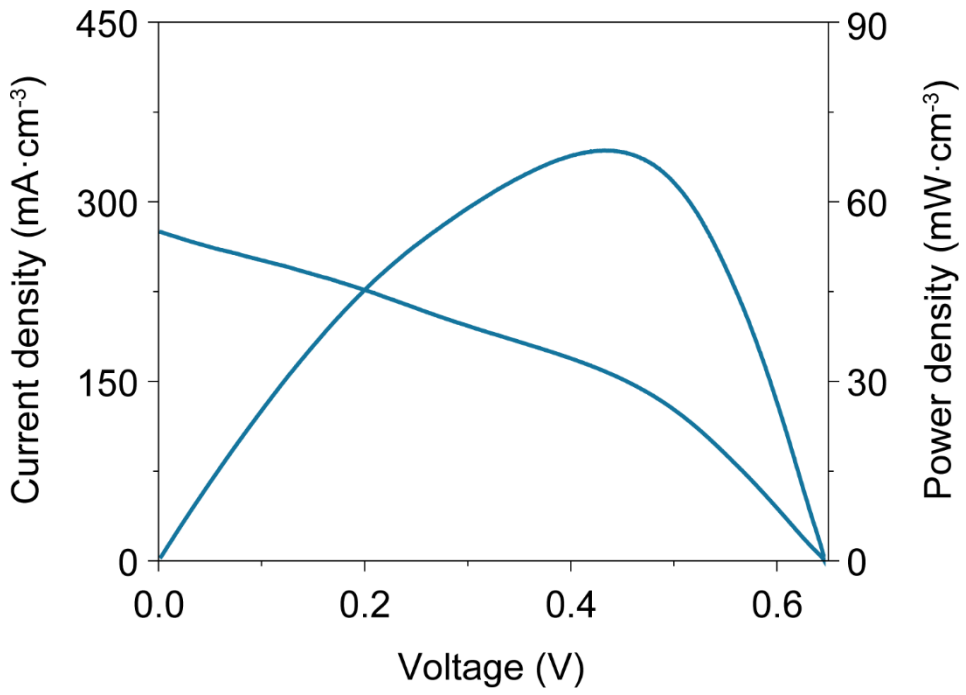

Figure S20. Polarization curves and power density curves of the BFC-PAI tested in PBS solution.

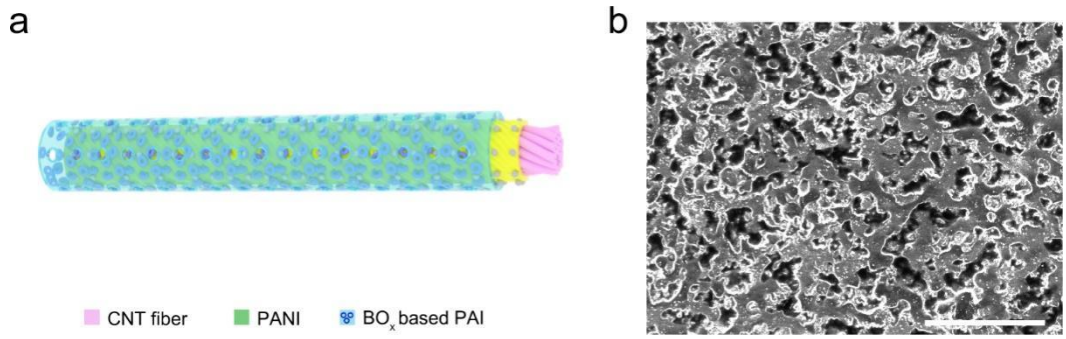

Figure S21. (a) Schematic illustration of the structure and **(b)** SEM image of the electrochemical glucose sensor. Scale bar, 50 μm.

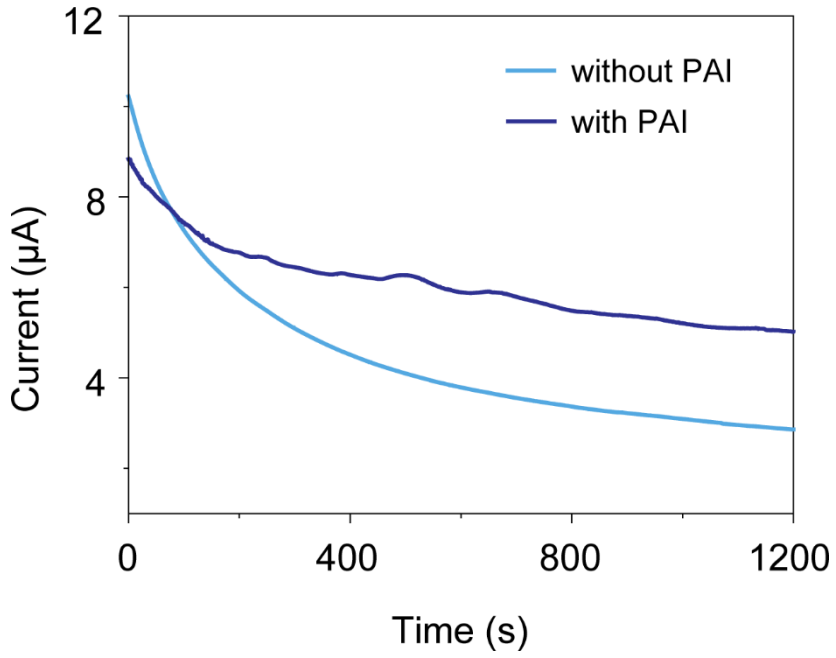

Figure S22. Potentiostatic polarization curve of the electrochemical glucose sensor with and without PAI tested in 5 mM glucose solution (0.1 M PBS buffer, pH 7.4).

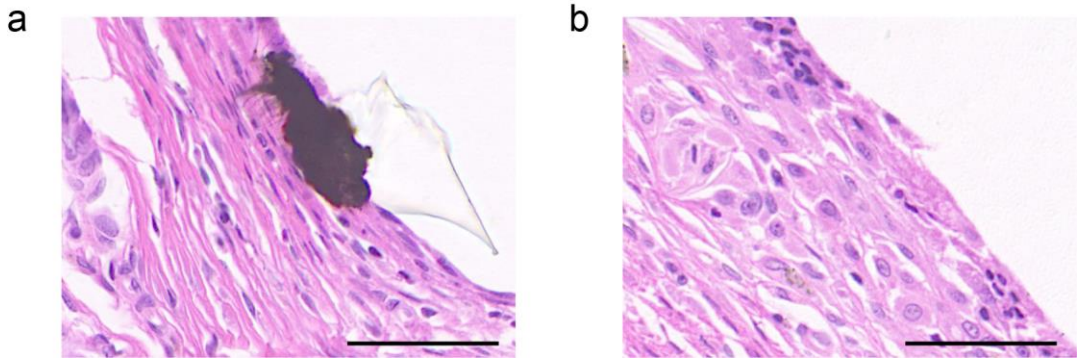

Figure S23. Representative H&E stained sections of the blood vessel with (**a**) implanted BFC-PAI for 45 days and (**b**) non-implanted control. Scale bar, 50 μm.

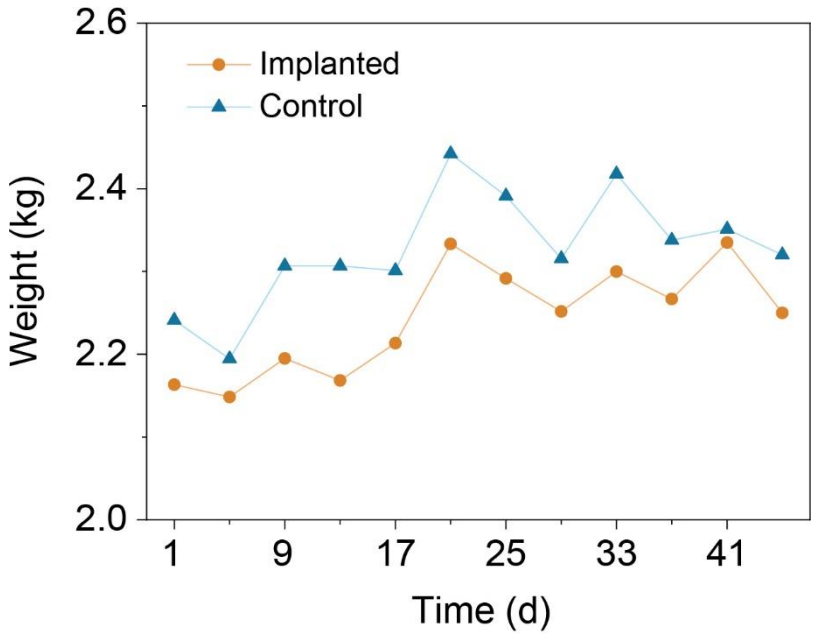

Figure S24. The weight change of rabbits after implanted with BFC-PAI in 45 days.

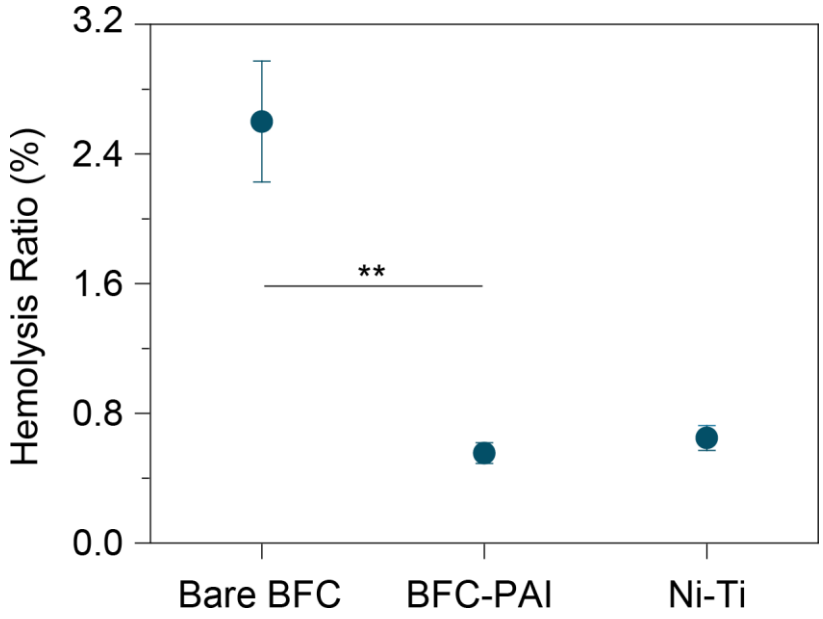

Figure S25. The hemolysis ratio of bare BFC, BFC-PAI and commercial Ni-Ti alloy.

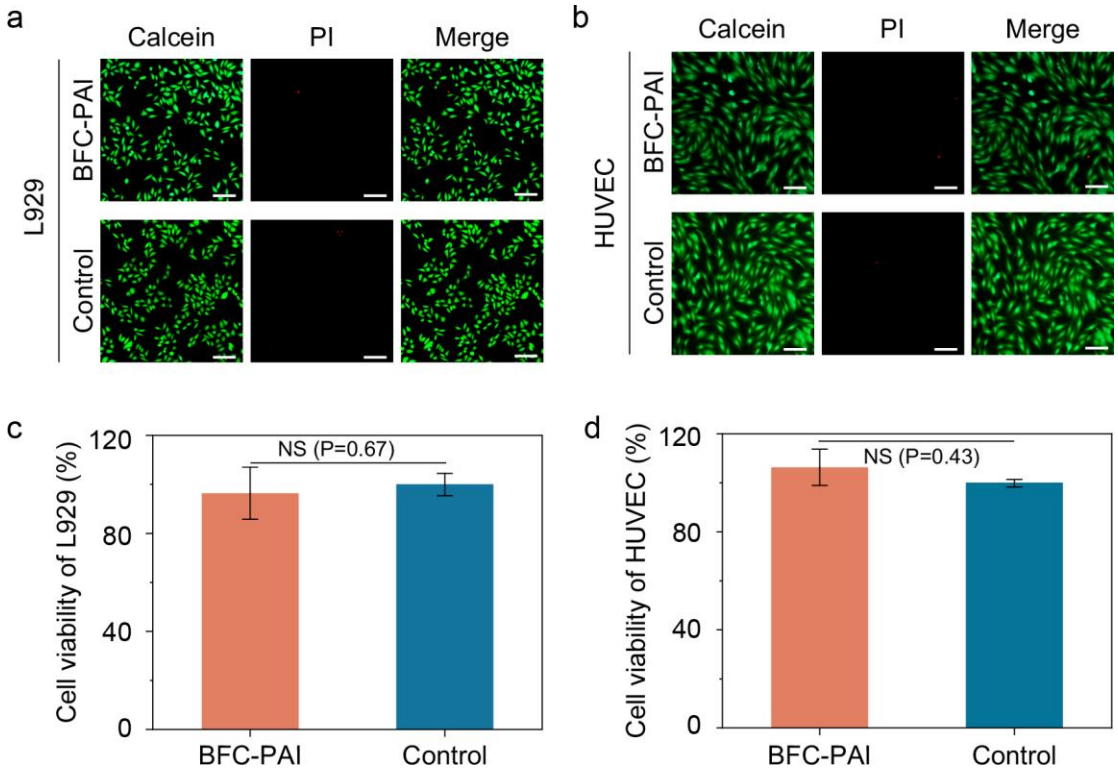

Figure S26. The effect of BFC-PAI on the proliferation of fibroblast L929 cells and HUVEC with glasses as control group. Representative fluorescence images of calcein and PI stained proliferating (**a**) L929 cells and (**b**) HUVEC. Scale bar, 100 μm. Green: living cells, calcein; red: dead cells, PI. The cell viability of (**c**) L929 cells and (**d**) HUVEC was measured by CCK-8 test. P value was calculated using One-way ANOVA.

Table S1. Comparison of the output power of our BFC-PAI with the previous implantable BFC.

Animals	Implant location	Bioanode	Biocathode	Power density ($mW \cdot cm^{-3}$)	Open-circuit voltage (V)	Ref.
Rat	Retroperitoneal space	Graphite/ubiquinone/GOx/glycerol	Graphite/quinone/hydroquinone, polyphenol oxidase/glycerol	0.02	0.27	[2]
Rat	Retroperitoneal space	Carbon felt/GOx/glycerol	Carbon felt/urease/glycerol	0.01	0.265	[2]
Clam	Hemolymph	ITO/MWCNT/PBSE/PQQ-GDH	ITO/MWCNT/PBSE/laccase	0.25	0.36	[3]
Snail	Hemolymph	MWCNT/PBSE/PQQ-GDH	MWCNT/PBSE/laccase	0.57	0.53	[4]
Cockroach	Hemolymph	Carbon fiber/trehalase-GOx/PVI-Os(dm-bpy)$_2$Cl/PEGDGE	Carbon fiber/PVI-Os(bpy)$_2$Cl/BOx /PEGDGE	0.011	> 0.2	[5]
Rat	Abdominal cavity	CNT/GOx	CNT/laccase	0.161	0.57	[6]
Rat	Jugular vein	Carbon fiber/neutral red/GOx/BSA	Carbon fiber/Pt NPs	0.15	0.125	[7]
Rat	Brain	Au/Au NPs/CDH/glutaraldehyde	Au/Au NPs/BOx	0.8	0.55	[8]
Rat	Retroperitoneal space	MWCNT/GOx/catalase/1, 4-naphtoquinone	MWCNT/laccase/chitosan	0.2	0.32	[9]

Rabbit	Abdominal cavity	MWCNT/GOx/catalase/ naphtoquinone	MWCNT/laccase/chitosan-genipin	0.016	0.42	[10]
Rabbit	Ear vein	CNT fiber/PMB/FADGDH based PAI	CNT fiber/2-ANT/BOx based PAI	76.6	0.62	This work

MWCNT: multi-walled carbon nanotube; PBSE: 1-pyrenebutanoic acid succinimidyl ester; PQQ-GDH: PQQ-dependent glucose dehydrogenase; PVI-Os(dm-bpy)$_2$Cl: poly(1-vinylimidazole)-bis(4, 4'-dimethyl-2, 2'-bipyridine-N, N')dichloroosmium-(III) chloride dihydrate; PVI-Os(bpy)$_2$Cl: poly(1-vinylimidazole)-bis(2, 2'-bipyridine-N, N')dichloroosmium-(III) chloride dihydrate; PEGDGE: poly (ethylene glycol) diglycidyl ether; BSA: bovine serum albumin; Au NPs: Au nanoparticles; CDH: cellobiose dehydrogenase

Table S2. The BSA adhesion ratio and FBG adhesion ratio of bare BFC, BFC-TAM, BFC-PAI and commercial antifouling materials Ni-Ti alloy.

Index	Sample	1	2	3	Average	Variance
BSA Adhesion Ratio (%)	Bare BFC	41.32	29.36	19.74	30.14	8.83
	BFC-TAM	10.78	11.91	9.11	10.60	1.15
	BFC-PAI	5.77	2.74	3.78	4.10	1.26
	Ni-Ti	9.21	9.04	10.88	9.71	0.83
FBG Adhesion Ratio (%)	Bare BFC	45.41	37.66	40.08	41.05	3.24
	BFC- TAM	20.33	26.74	23.99	23.69	2.63
	BFC-PAI	24.24	36.46	30.35	30.35	4.99
	Ni-Ti	28.30	30.77	38.02	27.87	4.12

Table S3. The platelet adhesion of bare BFC, BFC-TAM, BFC-PAI and commercial antifouling material of Ni-Ti alloy.

Sample	1	2	3	Average	Variance
Bare BFC	1.70	1.75	1.71	1.72	0.02
BFC- TAM	1.48	1.49	1.46	1.48	0.01
BFC-PAI	1.48	1.45	1.48	1.47	0.01
Ni-Ti	1.47	1.47	1.52	1.49	0.02

Table S4. Fluorescence intensity of biofouling from FBG protein formed on the electrode surface of bare BFC and BFC-PAI after soaking for different periods.

Sample	Time (h)	1	2	3	Average	Variance
Bare BFC	0.5	134.31	149.995	132.91	139.07	7.75
	2	137.175	172.593	142.914	150.89	15.52
	4	165.818	207.388	161.622	178.28	20.66
BFC-PAI	0.5	71.812	45.5	108.125	75.15	25.67
	2	84.909	89.143	96.048	90.03	4.59
	4	100.143	86.625	91.375	92.71	5.60

Table S5. The hemolysis ratio of bare BFC, BFC-PAI and commercial Ni-Ti alloy.

Sample	1	2	3	Average	Variance
Bare BFC	1.27	0.72	2.31	2.60	0.37
BFC-PAI	0.60	0.59	0.46	0.60	0.00
Ni-Ti	0.70	0.54	0.70	0.65	0.08

Table S6. The cell viability of L929 and HUVEC on BFC-PAI and control group.

Index	Sample	1	2	3	Average	Variance
Cell viability of L929 (%)	BFC-PAI	107.00	83.84	98.18	96.34	8.83
	Control	104.42	104.32	91.26	100.00	6.18
Cell viability of HUVEC (%)	BFC-PAI	113.73	91.90	113.25	106.29	10.18
	Control	98.53	101.35	100.12	100.00	1.15

Supplementary References

[1] L. Wang, S. Xie, Z. Wang, F. Liu, Y. Yang, C. Tang, X. Wu, P. Liu, Y. Li, H. Saiyin, S. Zheng, X. Sun, F. Xu, H. Yu, H. Peng, *Nat. Biomed. Eng.* **2020**, *4*, 159.

[2] P. Cinquin, C. Gondran, F. Giroud, S. Mazabrard, A. Pellissier, F. Boucher, J. P. Alcaraz, K. Gorgy, F. Lenouvel, S. Mathé, P. Porcu, S. Cosnier, *Plos one* **2010**, *5*, e10476.

[3] A. Szczupak, J. Halámek, L. Halámková, V. Bocharova, L. Alfonta, E. Katz, *Energy Environ. Sci.* **2012**, *5*, 8891.

[4] L. Halámková, J. Halámek, V. Bocharova, A. Szczupak, L. Alfonta, E. Katz, *J. Am. Chem. Soc.* **2012**, *134*, 5040.

[5] M. Rasmussen, R. E. Ritzmann, I. Lee, A. J. Pollack, D. Scherson, *J. Am. Chem. Soc.* **2012**, *134*, 1458.

[6] A. Zebda, S. Cosnier, J. P. Alcaraz, M. Holzinger, A. Le Goff, C. Gondran, F. Boucher, F. Giroud, K. Gorgy, H. Lamraoui, P. Cinquin, *Sci. Rep.* **2013**, *3*, 1516.

[7] F. C. P. F. Sales, R. M. Iost, M. V. A. Martins, M. C. Almeida, F. N. Crespilho, *Lab Chip* **2013**, *13*, 468.

[8] V. Andoralov, M. Falk, D. B. Suyatin, M. Granmo, J. Sotres, R. Ludwig, V. O. Popov, J. Schouenborg, Z. Blum, S. Shleev, *Sci. Rep.* **2013**, *3*, 3270.

[9] S. E. Ichi, A. Zebda, J. Alcaraz, F. Boucher, J. Boutonnat, P. Cinquin, D. K.

Martin, IEEE Conference on *Biomedical Engineering and Sciences* **2014**, 51.

[10] S. E. I. Ribault, J. P. Alcaraz, F. Boucher, B. Boutaud, R. Dalmolin, J. Boutonnat, P. Cinquin, A. Zebda, D. K. Martin, *Electrochim. Acta* **2018**, *269*, 360.